Liquid spring damper for vertical landing reusable launch vehicle under impact conditions

Shuai Yue[1], Branislav Titurus[2], Hong Nie[1], Ming Zhang[1]

Abstract: This research presents the modelling, experimental validation and analysis of the liquid spring damper under impact conditions during the symmetric vertical soft landing of a Reusable Launch Vehicle. A new nonlinear lumped parameter hydraulic model of a liquid spring damper is first established including the variable liquid bulk modulus, entrapped air, flow inertial effects and cavitation phenomena. Then, a simplified nonlinear model of the scaled Reusable Launch Vehicle test prototype is proposed. This dynamic model, which consists of a three degree-of-freedom main body and a single landing leg assembly with one liquid spring damper, is studied under impact conditions. The experimental prototype with the four nominally identical landing legs is experimentally studied. First, the quasi-static spring damper tests are conducted to identify the compressibility and friction parameters. Then, the Reusable Launch Vehicle prototype drop tests are performed to identify the liquid flow parameters, to validate the damper impact response characteristics and to evaluate the full prototype model through its comparison with the experimental data. It is found that a very good match can be established between the predicted and measured quasi-static damper responses. The local damper predictions also indicate good correlation with the impact test results. The landing prototype simulations indicate qualitatively correct predictions with the main observed discrepancies attributed to the simplified and potentially excessively stiff nature of the prototype model.

Keywords: *liquid spring; modelling; parameter identification; impact; vertical landing*

[1] State Key Laboratory of Mechanics and Control of Mechanical Structures, Nanjing University of Aeronautics and Astronautics, Nanjing 210016, China

[2] Corresponding Author, Department of Aerospace Engineering, University of Bristol, University Walk, Bristol, BS8 1TR, U.K, E-mail: brano.titurus@bristol.ac.uk

1. Introduction

As Reusable Launch Vehicle (RLV) can reduce the launching cost and improve the flight flexibility, many aerospace organizations consider RLV as a main development trend for the space transportation systems. After several successful industry-funded recovery tests, the vertical landing RLV has attracted public attention. Among all subsystems of vertical landing RLV, the landing gear system is one of the most important systems because its malfunction can lead to the failure of the entire mission [1]. Due to the uncertainties in the initial landing conditions and relatively high gravity center of the RLVs, the dampers are necessary and essential part in the landing gear system to reduce the landing impact and improve landing stability. Consequently, it becomes crucial to analyze dynamic performance of the dampers and their influence on the landing responses of vehicle during its touchdown.

Various types of dampers for vertical landing vehicles have been researched. The crushable metal damper is one of the widely used dampers. Wei et al. [2] and Yue et al. [3] studied the honeycomb attenuation capability under varying initial conditions through simulations and experiments. Witte [4] studied the probability of the landing failure of the planetary landing systems with the energy-absorbing honeycomb. Although the crushable metal damper is lightweight and reliable, the non-reusability restricts its implementation on the reusable landing gear system. Semi-active dampers are also broadly considered and applied in vehicle landing. Choi et al. [5] conducted research on the feasibility of using magneto-rheological fluid dampers on landers and helicopters. Despite that the semi-active dampers are adaptable under varying landing conditions, they are typically heavy, expensive and complex, resulting in relatively low reliability. Some other types of dampers investigated recently include the momentum exchange impact damper for planetary lander [6] and the electromagnetic damper in Mars hopper [7]. These dampers are still in the stage of laboratory research or small-scale experiments, with limited knowledge of their practical performance under various landing conditions. Compared with these dampers, the liquid spring damper possesses the features of high strength, good reliability and great compactness which are useful in landing gear system of the vertical landing RLVs. Therefore, this paper focuses on the touchdown analysis of the liquid spring damper.

The liquid spring dampers or hydraulic dampers have been considered in a wide range of areas. Sperling [8] established a dynamic landing model for the Surveyor landers with hydraulic shock absorbers and their landing stability was analyzed. Hong et al. [9], Samantaray [10] and Raja et al. [11]

investigated the attenuation performance of the liquid spring dampers with highly compressible fluids. Welsh [12] analyzed the dynamic characteristics of helicopter-used hydraulic damper with gas chamber and spring-assisted valve under low and high frequency excitations, both numerically and experimentally. Farjoud et al. [13] studied the characteristics of hydraulic damper as well. The constant liquid bulk modulus was used in their models to represent the compressibility of fluid under different pressures. By taking into account the entrapped air in the fluid, which has a great influence on the fluid bulk modulus during initial compression [14], Titurus [15], [16] and Gholizadeh et al. [17] introduced the effective bulk modulus in their models. With the consideration that the effective fluid bulk modulus would change with pressure and air content, Wang et al. [18] developed models with the effective bulk modulus being a function of the pressure and air content, with experiments conducted to validate the simulation model. In addition, a gaseous cavitation is an important issue that results in negative effects on the performance of hydraulic systems [19]. Its effects on hydraulic damper performance, especially on damping characteristics, have been investigated numerically and experimentally [20].

Following these investigations, a new nonlinear lumped parameter hydraulic model of the liquid spring damper is proposed. It includes the physical effects of the variable liquid bulk modulus, entrapped air, fluid flow inertial effects and cavitation phenomenon simultaneously. The main aim of this research is to evaluate the predictive quality and interpret the behavior of the liquid spring damper under impact conditions during the vertical landing scenario. To support this research, a dedicated scaled main body and four-legged landing gear RLV experimental prototype was developed and experimentally studied. A simplified three degree-of-freedom (3-DOF) model of the RLV prototype during its symmetric soft-landing is established and coupled with the liquid spring damper model. The selected model parameters are identified from experiments on the prototype and its four nominally identical liquid spring dampers. Among the novel aspects of this work is the development of the enhanced nonlinear liquid spring damper model, experiment-based parameter identification and model validation performed for a range of the test conditions and across the four nominally identical dampers under quasi-static and transient impact test conditions. This combined numerical-experimental approach to the study of the dampers under landing conditions therefore provides the reference simulation platform for further refined landing simulations and landing gear damper design studies.

The structure of the paper is as follows: Section 1 presents an overview of the relevant research

and the main contributions of this work. Sections 2 and 3 investigate the mathematical modelling of the RLV with the liquid spring dampers. The description of experiments, parameter identification and damper validation are included in section 4. Section 5 concludes this research with the validation study of the overall RLV prototype simulation.

2. Landing gear in the RLV test prototype

This section introduces the configuration of the landing gear for the vertical landing RLV and explains the working procedure of the landing gear. After this, the configuration of the liquid spring damper in landing gear is presented and its working principles are explained.

2.1 Overall scheme of landing gear

The overall scheme of the landing gear in the vertical landing RLV is shown in Figure 1. The architecture of this stowable four-legged landing gear system is motivated by the existing industry-based design. Each landing leg consists of the main strut, auxiliary strut and footpad.

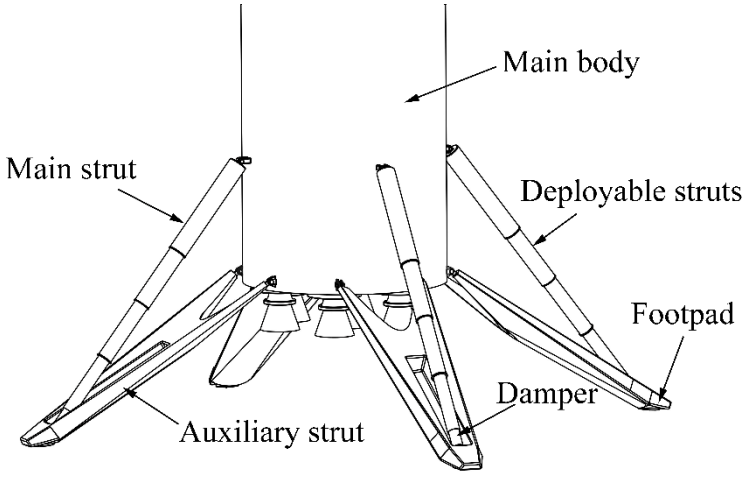

Figure 1 Overall architecture of the considered landing gear system

When the vehicle is launched, the landing gear system is in a retracted state, with the main strut in a stowed position. During the RLV landing, the main strut is extended by the deployable struts and the liquid spring damper, which is mounted at the lower end of the main strut, absorbs the landing energy through its compression and extension.

2.2 Working principle of the liquid spring damper

The configuration of the liquid spring damper and its hydraulic network are shown in Figure 2. The damper mainly includes the piston rod, piston, cylinder and sealing device. The piston rod is attached to the deployable telescopic strut while the cylinder is connected to the auxiliary strut by the revolute joint.

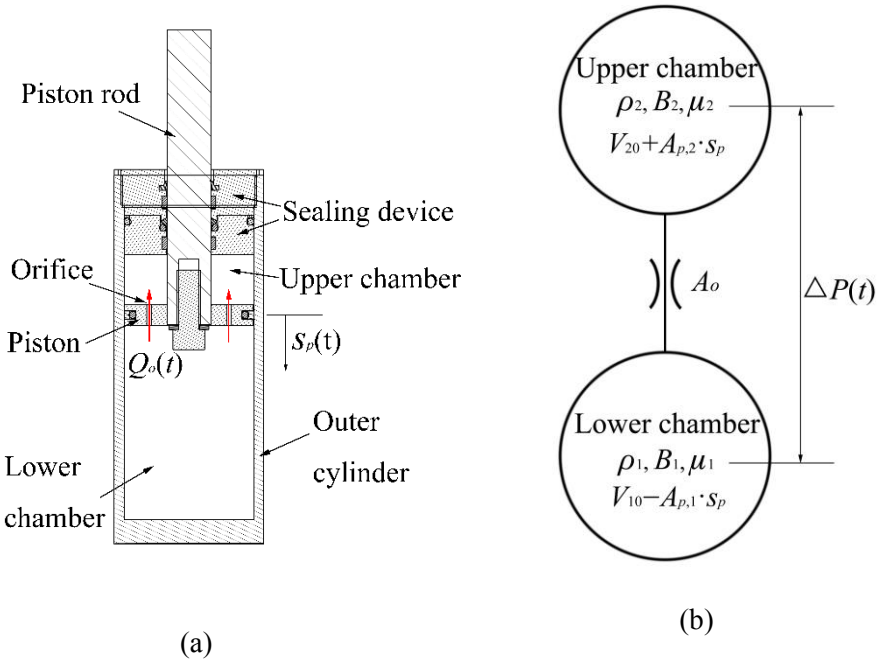

Figure 2 The schematic representation of the liquid spring damper:
(a) the structural configuration, (b) the hydraulic network

When the piston rod moves with the stroke s_p relative to the cylinder under the axial force F_h, the fluid flows through the orifice with the volumetric flow rate Q_o. This flow generates the pressure difference $\triangle P(t)$ between the upper and lower chambers. Meanwhile, with increasing piston stroke, the total volume of both chambers gets reduced and the liquid is pressurized due to the area difference between the two sides of the piston, which develops a spring force in the damper. Highly compressible *dimethyl silicone oil* is used as the working fluid in the liquid spring damper. In this work, the parameters ρ, B and μ denote the liquid or fluid density, the bulk modulus and the dynamic viscosity, respectively, and indices 1 and 2 are employed to distinguish the two chambers.

3. Nonlinear landing gear model

3.1 RLV dynamic model

The RLV dynamic model presented in this section is directly coupled with the liquid spring damper model to form an overall RLV landing simulation framework. The system shown in Figure 1 is considered during its symmetric soft landing. The symmetry consideration enables a relatively low order vertically moving RLV model which represents the landing mechanics of this configuration with a single modelled landing leg and its liquid spring damper.

The proposed 3-DOF model is shown in Figure 3. The vehicle is split into an upper and lower mass, which are, respectively, concentrated in the gravity center of the vehicle's main body and footpad. The upper mass with one vertical degree of freedom is connected to the two-degree-of-freedom lower mass by the main strut and auxiliary strut. The upper mass includes a quarter of main body, deployable struts, piston rod of the liquid spring damper and half-mass of the auxiliary strut in a single landing leg, while the lower mass contains the damper outer cylinder, half-mass of the auxiliary strut and the footpads in this landing leg. On touchdown, the contact forces from the ground are passed through the lower mass to the upper mass, causing the deflection of the main and auxiliary struts.

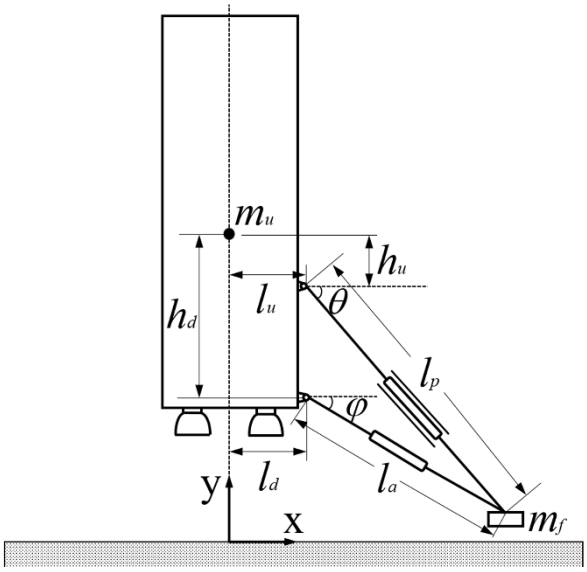

Figure 3 Geometry of the RLV vertical landing configuration

The governing equation of motion for the upper mass is given as follows:

$$m_u \frac{\mathrm{d}v_c}{\mathrm{d}t} = F_h \sin\theta - F_a \sin\varphi - m_u g \tag{1}$$

where m_u is the upper mass, g is the acceleration of gravity, v_c is the velocity of upper mass in vertical direction in the global coordinate frame, F_h and F_a are the axial forces of the main and auxiliary strut, respectively, θ and φ are the rake angle of main and auxiliary strut, respectively, which can be denoted as

$$\begin{aligned}\theta &= \arcsin\frac{y_c - h_u - y_f}{\sqrt{(x_f - l_u)^2 + (y_c - h_u - y_f)^2}} \\ \varphi &= \arcsin\frac{y_c - h_d - y_f}{\sqrt{(x_f - l_d)^2 + (y_c - h_d - y_f)^2}}\end{aligned} \tag{2}$$

where y_c is the vertical position of the upper mass gravity center, x_f and y_f represent the coordinates of the lower mass, h_u and l_u are the distances between the main body gravity center and the connection points between the main strut and main body in vertical and horizontal directions, respectively, h_d and l_d are the distances between the main body gravity center and connection point between the auxiliary strut and main body in vertical and horizontal directions, respectively.

The governing equation of motion for the lower mass is given as follows

$$\begin{aligned}m_d \frac{\mathrm{d}v_{xf}}{\mathrm{d}t} &= F_h \cos\theta - F_a \cos\varphi + F_t \\ m_d \frac{\mathrm{d}v_{yf}}{\mathrm{d}t} &= -F_h \sin\theta + F_a \sin\varphi + F_n - m_d g\end{aligned} \tag{3}$$

where m_d is the lower mass, v_{yf} and v_{xf} are the velocities of lower mass in vertical and horizontal directions, respectively, F_n and F_t are the contact forces from the ground in the vertical and horizontal directions, respectively.

Then, the stroke of the main strut s_p can be expressed as:

$$s_p = l_{p0} - \sqrt{(x_f - l_u)^2 + (y_f + h_u - y_c)^2} \tag{4}$$

where l_{p0} is the length of the main strut at fully extended configuration.

The velocity of the main strut v_p can be deduced by differentiating equation (4) with respect to time

$$v_p = -\frac{(x_f - l_u)\cdot v_{xf} + (y_f + h_u - y_c)\cdot(v_{yf} - v_c)}{l_{p0} - s_p}. \tag{5}$$

Similarly, the stroke and velocity of the auxiliary strut s_a, v_a are

$$
\begin{aligned}
s_a &= l_{a0} - \sqrt{(x_f - l_d)^2 + (y_f + h_d - y_c)^2} \\
v_a &= -\frac{(x_f - l_d)\cdot v_{xf} + (y_f + h_d - y_c)\cdot (v_{yf} - v_c)}{l_{a0} - s_a}
\end{aligned} \tag{6}
$$

where l_{a0} is the initial length of the auxiliary strut.

3.2 Main strut model

The deflection of the main strut is mainly due to the compression of the hydraulic damper. Therefore, this section focuses on the establishment of the nonlinear liquid spring damper model. The compressibility of fluid, entrapped air, fluid flow inertial effects and cavitation phenomena are included in this mathematical model with the following assumptions:

1. The temperature is assumed to be constant and the deformation of the damper's outer cylinder is ignored during the touchdown.
2. The entrapped air and vapor are uniformly distributed in the liquid. The pressure, fluid density and effective bulk modulus are defined as lumped parameters for each working chamber.
3. The vapor pressure of the liquid is chosen as a conservative estimate of 0.05 bar for predicting the onset of cavitation. The vapor phase forms and collapses instantaneously when the pressure is below and above, respectively, the vapor pressure [21] and it behaves as an ideal gas [22].
4. The volumetric reduction of entrapped air due to air dissolving into liquid is negligible.
5. The air undergoes isothermal process during quasi-static compression tests and polytropic process during touchdown tests [23].

In this paper, the liquid refers to the *dimethyl silicone oil*, while the fluid refers to the mixture of silicone oil, entrapped air and vapor (if present).

3.2.1 Liquid spring damper model with compressible fluid

Based on the mass conservation principle, the relationship for the general i^{th} variable fluid volume can be denoted as follows [24]

$$
\frac{\mathrm{d}V_i}{\mathrm{d}t} + \frac{V_i}{B_i(P_i)}\frac{\mathrm{d}P_i}{\mathrm{d}t} = \frac{1}{\rho_i}\left(\sum_{(j)}\dot{m}_{in,j} - \sum_{(k)}\dot{m}_{out,k}\right) \tag{7}
$$

where V_i is the volume of the i^{th} chamber, P_i is the pressure of the i^{th} chamber, $B_i(P_i)$ is the fluid bulk

modulus of the i^{th} chamber under pressure P_i, ρ_i is the fluid density in the i^{th} chamber, $\dot{m}_{in,j}$ and $\dot{m}_{out,k}$ are the fluid mass flow rates of the j^{th} inflow and k^{th} outflow, respectively.

With reference to equation (7) and Figure 2(b), the following equations can be written for chamber 1 and 2

$$\begin{aligned} \dot{V}_1 + V_1\dot{P}_1 / B_1 &= -\dot{m}_{out,1} / \rho_1 \\ \dot{V}_2 + V_2\dot{P}_2 / B_2 &= \dot{m}_{in,2} / \rho_2 \end{aligned} \tag{8}$$

where an overdot represents a derivative with respect to time.

Based on Figure 2(a), volumes V_1 and V_2 are defined as follows

$$\begin{aligned} V_1 &= V_{01} - A_{P,1}s_p, \qquad \dot{V}_1 = -A_{P,1}v_p \\ V_2 &= V_{02} + A_{P,2}s_p, \qquad \dot{V}_2 = A_{P,2}v_p \end{aligned} \tag{9}$$

where V_{01} and V_{02} are the initial or reference volumes of the respective chambers, $A_{P,1}$ and $A_{P,2}$ are the wetted piston areas in chamber 1 and 2, respectively.

According to Figure 2(b), the outflow path in chamber 1 is the same as the inflow path in chamber 2. It is assumed that the corresponding flow is incompressible, $\dot{m}_{in,1}(t) = \dot{m}_{out,2}(t) \equiv \dot{m}_{12}(t)$. The mass and the corresponding volumetric flow rate model between the working chambers 1 and 2 is expressed as $\dot{m}_{12} = \rho_{12}Q_o(\rho_{12}, \mu_{12})$, where $\rho_{12} \equiv \rho_{avg} = (\rho_1 + \rho_2)/2$ is the chosen flow path fluid density due to density discontinuity between the compressible working volumes with $\rho_1 \neq \rho_2$, Q_o, μ_{12} are the path's volumetric fluid flow rate and the corresponding dynamic viscosity, respectively. This volume coupling condition ensures the conservation of mass in the modelled damping system.

The resulting differential equations for the pressures in chamber 1 and 2 are

$$\begin{aligned} \frac{\mathrm{d}P_1}{\mathrm{d}t} &= \frac{B_1}{V_1}\left(A_{P,1}v_P - \frac{\rho_{avg}}{\rho_1} \cdot Q_o \right) \\ \frac{\mathrm{d}P_2}{\mathrm{d}t} &= \frac{B_2}{V_2}\left(-A_{P,2}v_P + \frac{\rho_{avg}}{\rho_2} \cdot Q_o \right) \end{aligned}. \tag{10}$$

Equation (10) represents the central part of the spring damper model. It is augmented by the additional fluid effects in the following sections of this chapter.

3.2.2 Model of the pressure losses with inertial effects

Based on the unsteady Bernoulli equation [25], the pressure drop across the orifice $P_1 - P_2$ consists of the laminar and turbulent pressure losses ΔP_f and inertance pressure drop ΔP_i. The standard combined laminar-turbulent pressure loss model [24] is related to the flow rate as follows

$$\Delta P_f = \frac{8\pi l_h \mu_{avg}}{A_o^2} Q_o + \frac{\rho_{avg}}{2(C_d A_o)^2} Q_o |Q_o| \tag{11}$$

where l_h is the length of the orifice, A_o is the orifice area, C_d is the discharge coefficient, $\mu_{avg} \equiv \mu_{12}$, where $\mu_{avg} = (\mu_1 + \mu_2)/2$, is the dynamic viscosity of fluid in the orifice, μ_{avg} is selected to be the average viscosity of the two chambers due to viscosity discontinuity between the chambers. The specific dynamic viscosity equation is included in the following section 3.2.4.

The inertance pressure drop [25], [26] can be interpreted as the pressure differential required to accelerate the fluid column located in the flow path. This flow path is represented by the orifice in this work. This model is represented as follows

$$\Delta P_i = I_h \frac{\mathrm{d}Q_o}{\mathrm{d}t} = \frac{\rho_{avg} l_h}{C_c A_o} \frac{\mathrm{d}Q_o}{\mathrm{d}t} \tag{12}$$

where I_h is the inertance of fluid in the orifice and C_c is the orifice jet contraction coefficient [25].

From equations (11) and (12), the fluid flow model is

$$\frac{dQ_o}{dt} = \frac{1}{I_h}\left(P_1 - P_2 - \frac{8\pi l_h \mu_{avg}}{A_o^2} Q_o - \frac{\rho_{avg}}{2(C_d A_o)^2} Q_o |Q_o| \right) \tag{13}$$

where $P_1 - P_2 = \Delta P_f + \Delta P_i$ is the total pressure difference across the orifice or other fluid flow paths.

3.2.3 Model of cavitation

The cavitation is a complex phenomenon which involves the vapor formation, its growth and collapse. During the landing impact with high touchdown velocities, the local pressures inside the hydraulic damper can fall close to the vapor pressure where the cavitation is expected to occur [27].

Based on the previous assumptions, an additional working volume state variable which represents the vapor volume V_v is introduced and used to detect the cavitation and its evolution in time. For a given

time instant, the mass balance, in a working volume with the non-dissolved air-liquid mixture and liquid vapor which is characterized by the ideal gas law, is used to define the vapor volume as

$$V_v = \frac{m_f - \rho_m(P_v)\,V}{(M_v P_v)/(RT) - \rho_m(P_v)} \tag{14}$$

where $\rho_m(P_v)$ is the varying density of the air-liquid mixture, m_f and V are, respectively, the total mass and total volume of the working chamber under consideration, M_v is the constant molar mass of the liquid vapor, P_v is the constant vapor pressure of the liquid, R is the universal gas constant and T is the absolute ambient temperature.

The temporal variation of the j^{th} vapor volume V_{vj}, $j=1,2$, can be attained by differentiating equation (14) with respect to time. With this additional modelled phenomenon, each working chamber is characterized by a pair of states P_j, V_{vj}, $j=1,2$. It is assumed that the minimum pressure in any chamber P_j is equal to the vapor pressure. After this condition is reached, i.e. $P_j = P_v$ and $\dot{P}_j < 0$, the chamber pressure remains constant while the vapor volume starts to increase

$$\begin{aligned} &\frac{\mathrm{d}P_j}{\mathrm{d}t} = 0, \\ &\frac{\mathrm{d}V_{vj}}{\mathrm{d}t} = \frac{(-1)^{j+1}}{(M_v P_v)/(RT) - \rho_{mj}(P_v)} \left(\rho_{avg} Q_j - \rho_{mj}(P_v) \frac{\mathrm{d}V_j}{\mathrm{d}t} \right). \end{aligned} \tag{15}$$

Similarly, when the chamber pressure is above the vapor pressure and the vapor volume becomes zero, i.e. $P_j \geq P_v$ and $V_{vj} = 0$, the j^{th} chamber pressure in equation (10) is used to calculate the chamber pressure P_j, with $\mathrm{d}V_{vj}/\mathrm{d}t = 0$.

3.2.4 Model of density, effective bulk modulus and viscosity

The presence of entrapped air bubbles and vapor in liquid can significantly influence the density, effective bulk modulus and viscosity of fluid [17]. Therefore, it is necessary to obtain these parameters depending on two different circumstances: 1. Only air bubbles exist in the working volumes, 2. Both air bubbles and vaporized liquid exist in the working volumes. For simplicity, the use of the chamber subscript *j* is dropped in this section.

Case 1: Only air bubbles

For convenience of derivation, a unit volume of liquid at the atmospheric pressure P_{atm} is considered, that is $V_{liq}(P_{atm})$=1. The air content x_a is defined as

$$x_a = \frac{V_{air}(P_{atm})}{V_{air}(P_{atm})+1} \tag{16}$$

where $V_{air}(P_{atm})$ is the volume of entrapped air at P_{atm}.

Then, the fluid mass m_{fluid} can be obtained as

$$m_{fluid} = \rho_{liq}(P_{atm}) + \frac{x_a}{1-x_a}\rho_{air}(P_{atm}) \tag{17}$$

where $\rho_{liq}(P_{atm})$ is the density of pure liquid under atmospheric pressure, $\rho_{air}(P_{atm})$ is the density of air in the fluid under atmospheric pressure.

The density of fluid under a certain pressure $\rho_{fluid}(P)$ is

$$\rho_{fluid}(P) = \frac{m_{fluid}}{V_{liq}(P)+V_{air}(P)} \tag{18}$$

where $V_{liq}(P)$ and $V_{air}(P)$ are the volume of liquid and air under a certain pressure P, respectively.

With the mass conservation of liquid, $V_{liq}(P)$ can be attained as

$$V_{liq}(P) = \frac{\rho_{liq}(P_{atm})}{\rho_{liq}(P)} \tag{19}$$

where $\rho_{liq}(P)$ is the density of liquid under a certain pressure P.

With the assumption of ideal gas, $V_{air}(P)$ can be obtained as

$$V_{air}(P) = V_{air}(P_{atm})\cdot\left(\frac{P_{atm}}{P}\right)^{\frac{1}{\gamma}} = \frac{x_a}{1-x_a}\cdot\left(\frac{P_{atm}}{P}\right)^{\frac{1}{\gamma}} \tag{20}$$

where γ is the polytropic exponent.

The bulk modulus of liquid under pressure P, $B_{liq}(P)$, which is assumed to change linearly with pressure, following the relationship [28], is

$$B_{liq}(P) = C_B\cdot(P-P_{atm}) + B_{liq}(P_{atm}) \tag{21}$$

where C_B is the coefficient representing the increment of bulk modulus with increasing pressure.

Based on the definition of the tangent bulk modulus for fluid [29], the liquid bulk modulus B_{liq} can be integrated with respect to the density of liquid under pressure P, $\rho_{liq}(P)$. Then $\rho_{liq}(P)$ can be obtained as

$$\rho_{liq}(P)=\rho_{liq}(P_{atm})\cdot\left(\frac{B_{liq}(P)}{B_{liq}(P_{atm})}\right)^{\frac{1}{C_B}}. \tag{22}$$

Finally, by employing equations (17), (19), (20) and (22), equations (18) can be transformed to the following form

$$\rho_{fluid}(P)=\frac{(1-x_a)\,\rho_{liq}(P_{atm})+x_a\,\rho_{air}(P_{atm})}{(1-x_a)\cdot\left(\frac{B_{liq}(P)}{B_{liq}(P_{atm})}\right)^{-\frac{1}{C_B}}+x_a\left(\frac{P_{atm}}{P}\right)^{\frac{1}{\gamma}}}. \tag{23}$$

Based on this, the effective fluid bulk modulus under pressure P, $B_{fluid}(P)$ is

$$B_{fluid}(P)=\frac{\rho_{fluid}(P)}{\frac{\partial\rho_{fluid}(P)}{\partial P}}=\frac{(1-x_a)\cdot\left(\frac{B_{liq}(P)}{B_{liq}(P_{atm})}\right)^{-\frac{1}{C_B}}+x_a\left(\frac{P_{atm}}{P}\right)^{\frac{1}{\gamma}}}{\frac{1-x_a}{B_{liq}(P_{atm})}\cdot\left(\frac{B_{liq}(P)}{B_{liq}(P_{atm})}\right)^{\frac{-1-C_B}{C_B}}+\frac{x_a}{P\gamma}\left(\frac{P_{atm}}{P}\right)^{\frac{1}{\gamma}}}. \tag{24}$$

The effective fluid viscosities in chambers 1 and 2 with entrained air are assumed to change with their respective pressures [30]. Then, the average fluid viscosity μ_{avg} through the orifice is obtained from the individual effective fluid viscosities in chambers 1 and 2

$$\mu=\mu_l\left(1+K_\mu\frac{V_{air}(P)}{V_{air}(P)+V_{liq}(P)}\right) \tag{25}$$

where μ_l is the viscosity of liquid, K_μ is a coefficient based on experiments by Hayward as referred in [30].

Case 2: Air bubbles and vaporized liquid

When cavitation occurs, a volume of vaporized liquid is produced. Under this condition, it is assumed that there is liquid, air and vaporized liquid coexisting and uniformly distributed in the fluid. The unit liquid volume assumption is still used to derive the following equations. The fluid mass is the same as that in equation (17) and the fluid density can be written as follows

$$\rho_{fluid}(P)=\frac{(1-x_a)\rho_{liq}(P_{atm})+x_a\rho_{air}(P_{atm})}{(1-x_a)(V_{liq}(P)+V_{air}(P))\cdot V/(V-V_v)} \tag{26}$$

where $V_{air}(P)$ is presented in equation (20), V_v is obtained from equation (15) and $V_{liq}(P)$ can be written as

$$V_{liq}(P)=\frac{(V-V_v)\cdot\rho_{liq}(P_{atm})-V_{air}(P)\cdot V_v\cdot(M_vP_v)/(RT_0)}{(V-V_v)\cdot\rho_{liq}(P)+V_v\cdot(M_vP_v)/(RT_0)} \tag{27}$$

where T_0 is the ambient temperature, V is the total volume of chamber.

The effective bulk modulus of fluid under cavitation conditions can be deduced as

$$B_{fluid}(P)=\frac{\rho_{fluid}(P)}{\frac{\partial\rho_{fluid}(P)}{\partial P}}=-\frac{(V_{liq}(P)+V_{air}(P))\cdot\frac{V}{V-V_v}}{\partial((V_{liq}(P)+V_{air}(P))\cdot\frac{V}{V-V_v})/\partial P}=-\frac{V_{liq}(P)+V_{air}(P)}{\partial(V_{liq}(P)+V_{air}(P))/\partial P} \tag{28}$$

When excluding the vapor phase and under the vapor pressure, the density of air-liquid mixture $\rho_m(P_v)$ used in equation (14) can be deduced as follows

$$\rho_m(P_v)=\frac{\rho_{liq}(P_{atm})+\frac{x_a}{1-x_a}\cdot\rho_{air}(P_{atm})-\frac{V_v\cdot(V_{liq}(P_v)+V_{air}(P_v))}{V-V_v}\cdot\frac{M_vP_v}{RT_0}}{V_{liq}(P_v)+V_{air}(P_v)} \tag{29}$$

Assuming that $V_v/(V-V_v)\ll 1$, $(M_vP_v)/(RT_0)\ll\rho_{liq}(P_{atm})$ and $(M_vP_v)/(RT_0)\ll\rho_{liq}(P_v)$, it can be further assumed from equation (27) that $V_{liq}(P_v)=\rho_{liq}(P_{atm})/\rho_{liq}(P_v)$. With these assumptions and based on equation (29), it can be obtained that $\mathrm{d}\rho_m(P_v)/\mathrm{d}t=0$. This development further facilitates the derivative of V_v with respect to time in equation (15).

By using equation (25) and considering the vapor phase as a part of the chamber's entrained air, the effective viscosity under cavitation conditions is deduced as

$$\mu=\mu_l\left(1+K_\mu\frac{V\cdot V_{air}(P)+V_v\cdot V_{liq}(P)}{V\cdot(V_{air}(P)+V_{liq}(P))}\right). \tag{30}$$

3.2.5 Model of friction

When calculating the friction force between the piston, piston rod and cylinder, the modified *Reset Integral Friction Model* [31] is employed. The nominal model can represent the stick-slip friction

phenomenon while retaining a good computational efficiency. The Stribeck effect is also considered to represent the variation of the friction force with the relative velocity v_p between the piston and cylinder [32]. The side load between the piston and cylinder is assumed to be negligible because of the landing leg configuration shown in Figure 1.

An additional state variable s_r is introduced to monitor the friction state and to enable computation of the friction force F_f. The friction state s_r depends on the relative velocity between the piston and cylinder v_p and an additional stick-slip friction condition. The friction state variable is equal to its last computed value when in the slip zone and its time derivative is equal to v_p when in the stick zone. The slip stage is detected when $v_p s_r > 0$ and $|s_r| \geq s_{r0}$ where the friction state variable is

$$\dot{s}_r = 0 . \tag{31}$$

When in the stick zone, the friction state variable is defined as follows

$$\dot{s}_r = v_P . \tag{32}$$

When considering the Stribeck effect, the friction forces for sticking and slipping responses are obtained through detecting whether the friction state variable s_r reaches the threshold displacement value s_{r0}

$$F_f = \begin{cases} K_r(1+a_r)s_r + C_r\dot{s}_r & |s_r| < s_{r0} \\ K_r(1+a_r \cdot \exp(-|v_p|/b_{strib})) \cdot s_r & |s_r| \geq s_{r0} \end{cases} \tag{33}$$

where K_r is the spring rate which determines the restoring part of the force, a_r represents the increase of the force that occurs during the sticking response mode, C_r is the damping coefficient during the sticking mode used to prevent non-physical oscillations, b_{strib} is a positive constant which represents the rate of the dynamic friction force variation with the relative velocity v_p. In addition, the friction force between the cylinder and seal is related to the chamber pressures [33]. In this work, K_r is assumed to change linearly with the reference chamber pressure following the relationship

$$\begin{aligned} K_r(P) &= K_{r0} + C_k P_r \\ P_r &= \begin{cases} P_1 - P_{atm} & P_1 \geq P_2 \\ P_2 - P_{atm} & P_1 < P_2 \end{cases} \end{aligned} \tag{34}$$

where K_{r0} is the initial value under atmospheric pressure and C_k represents the rate of change in K_r with the reference chamber pressure. Both parameters are determined through parameter identification.

3.3 Auxiliary strut model

Axial stiffness and damping are introduced to establish the simplified model of the auxiliary strut. Referring to the expression for the spring-damper force model [34], the relationship between the auxiliary strut force and its axial deflection is denoted as follows

$$F_a = K_a \left| s_a \right|^{e_k} \cdot \mathrm{sign}(s_a) + C_a v_a \tag{35}$$

where $K_a = E_a A_{eff} / l_{a0}$ and $C_a = 2\eta\sqrt{m_d K_a}$ are the axial stiffness and damping coefficient of the auxiliary strut, respectively, A_{eff} is the effective area of auxiliary strut, E_a is the effective elastic modulus of the auxiliary strut material, η is the damping ratio, e_k is the exponential coefficient of the nonlinear strut spring force, which is introduced to represent the stiffness hardening effect with increasing deflection due to elastic washers and, approximately, gaps and freeplay in the connection joint, sign(°) is the signum function.

3.4 Footpad-ground contact model

The footpad-ground contact force is simulated by employing a spring-damper model for the normal contact force F_n and a friction model for the friction force F_t.

The spring-damper model considers the normal penetration depth and velocity through the ground. The normal contact force F_n is attained from the penetration of the footpad as follows

$$F_n = \begin{cases} K_g \delta_F^{e_n} + C_{gmax}\,\mathrm{ramp}(\delta_F)\cdot\dot{\delta}_F & \delta_F > 0 \\ 0 & \delta_F \le 0 \end{cases} \tag{36}$$

where K_g is the ground spring constant, e_n is the exponential coefficient of the penetration depth, δ_F is the footpad penetration depth, $C_{g\max}$ is the maximum damping coefficient of ground contact, ramp(δ_F) is a ramp function which increases from 0 to 1 during $[0, \delta_{\mathrm{pen}}]$. $C_{g\max}\cdot$ramp(δ_F) represents the variable ground damping coefficient throughout footpad penetration. When the penetration depth δ_F increases from 0 to δ_{pen}, the variable damping coefficient increases from 0 to $C_{g\max}$. When δ_F is greater than δ_{pen}, the damping coefficient remains at the constant value $C_{g\max}$. Therefore, δ_{pen} is the minimum penetration depth when $C_{g\max}\cdot$ramp(δ_F) reaches $C_{g\max}$. The use of the variable damping coefficient ensures stable calculations by introducing smooth and depth-dependent change of the damping part of F_n during the contact stages.

The *Reset Integral Friction Model* [31] with the Stribeck effect is used in modified form here to model the contact friction between the footpad and ground. The contact tangential friction force F_t between the footpad and ground uses equation (33) with the new state variable s_{rf}. Additionally, the spring rate parameter in this case is defined as

$$K_r = \left|\mu_c F_n\right| / s_{rf\,0} \tag{37}$$

where μ_c is the friction coefficient of the footpad-ground contact.

3.5 Nonlinear vertical landing RLV model

For the computations, the overall and liquid spring damper models are implemented in MATLAB [35] and its Ordinary Differential Equation (ODE) solver capabilities are used to compute the required transient temporal behavior. The full RLV landing prototype model, Figure 3, uses the mechanical states $\mathbf{x}_m$, hydraulic states $\mathbf{x}_h$ and friction states $\mathbf{x}_f$ to represent the system dynamics as

$$\dot{\mathbf{x}} = \mathbf{f}(t, \mathbf{x}) \tag{38}$$

where the solution time interval is $t \in [0, t_{max}]$, the full state vector is $\mathbf{x} = [\mathbf{x}_m, \mathbf{x}_h, \mathbf{x}_f] \in \mathbb{R}^{13}$ and the individual states are

$$\mathbf{x}_m = [y_c, v_c, x_f, v_{xf}, y_f, v_{yf}], \quad \mathbf{x}_h = [V_{v1}, P_1, V_{v2}, P_2, Q_o], \quad \mathbf{x}_f = [s_r, s_{rf}]. \tag{39}$$

The flow chart demonstrating the integration of all relevant equations is presented in Figure 4.

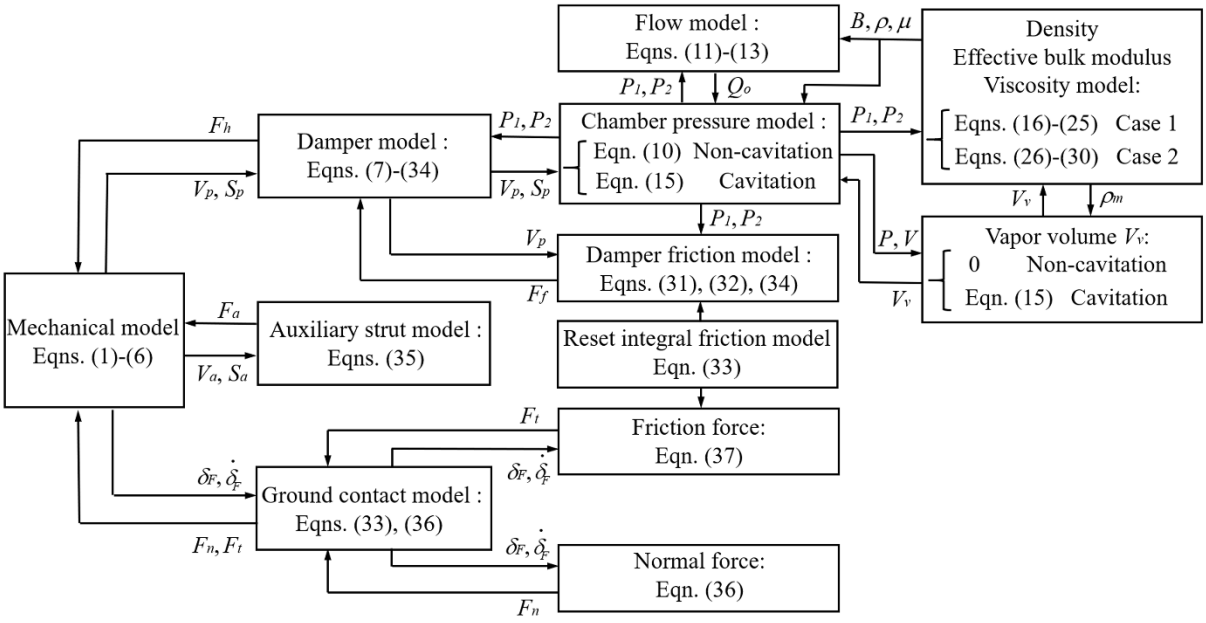

Figure 4 The overall model flow chart

From Figure 4, the mechanical model and its states $\mathbf{x}_m$ is characterized by equations (1)-(6), while the damper model and its states $\mathbf{x}_h$ is characterized by equations (7)-(34). The mechanical model is coupled with the damper model through the damper force $F_h = A_{P,1}P_1 - A_{P,2}P_2 + F_f$ and the damper model is linked with the mechanical model through the kinematic piston inputs s_P, v_p derived from the mechanical states $\mathbf{x}_m$. Assuming symmetric landing conditions, the upper mass of the mechanical model is taken as a quarter of the vehicle's actual mass. The pressure difference in the model originates from the two identical orifices present in the real damper. The damper model consists of three parts: flow model (equations (11)-(13)) with its state Q_o; chamber pressure model (equations (10)) with its states P_1, P_2; and damper friction model (equations (31)-(34)) with its state s_r. The density, effective bulk modulus and viscosity models (equations (16)-(30)) calculate parameters ρ, B and η, respectively, for each chamber under its specific pressure obtained from the chamber pressure model. The vapor volume model (equation (15)) is responsible for calculating the vapor volume under the conditions of cavitation and non-cavitation. The auxiliary strut model is linked with the mechanical model through the kinematic inputs s_a, v_a and force output F_a defined in equation (35). The ground contact model (equations (33), (36)-(37)), which contains the normal force component and the friction force component with state s_{rf}, is integrated with the mechanical model through the footpad penetration δ_F, $\dot{\delta}_F$ and contact force output F_t, F_n. A variable step size Matlab ODE solver *ode45* [35], which implements a pair of the explicit Runge-Kutta methods, was used to solve the full system of the formulated ODEs. To ensure the stable and robust solver performance, and in response to the conditional behavior implied in the cavitation model, the full dynamic model was solved using the Matlab's "event" detection functionality with repeated ODE solver restarts until reaching the required simulation time $t_{\max}$.

4. Parameter identification and validation analysis

4.1 Prototype design and test scheme

The prototype of the vehicle's main body with the landing system is designed, built and then tested to enable parameter identification and model validation. The test campaign was completed at the State Key Laboratory of Mechanics and Control of Mechanical Structures in Nanjing University of

Aeronautics and Astronautics. Initially, the quasi-static tests are conducted to identify the liquid spring damper compressibility and friction parameters. The axial forces of the four nominally identical hydraulic dampers are measured and recorded by the computer-controlled universal testing machine by SANS shown in Figure 5. During the tests, the constant speed compression and retraction inputs are applied to the damper pistons to obtain the quasi-static compressibility and friction-dominated force responses.

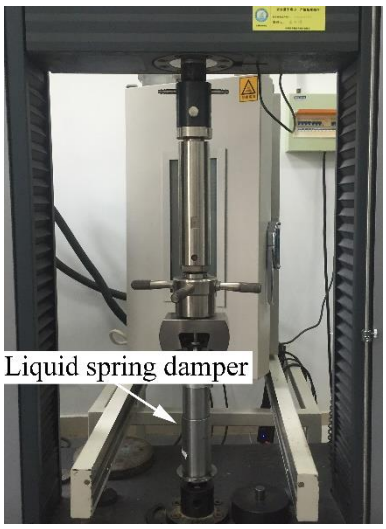

Figure 5 Quasi-static compression test configuration

After this, the symmetric soft-landing drop tests utilizing the configuration shown in Figure 6 are used to produce highly dynamic landing responses suitable for the flow parameter identification and, subsequently, for overall model validation. The test system mainly includes the vehicle main body, landing system, lifting-releasing system, measurement and data acquisition system. The prototype is elevated to the predetermined height by the electromagnet-controlled lift-releasing system prior to each drop test. The power cut in the electromagnet device is used to initiate the drop tests and give the prototype its initial landing velocity.

During these tests, the stroke of the four hydraulic dampers is measured by the displacement transducers DH801-750 provided by Donghua company, which are installed on each landing strut. The axial forces transferred by the hydraulic dampers and auxiliary struts are obtained from the force transducers L2030 by Yangzhou City Electronic Science and Technology Corporation shown in Figure 6. The vertical acceleration of the vehicle is measured by a piezoelectric accelerometer 1A101 of Donghua company mounted at the top of the main body. The data acquisition equipment used during

the tests is the dynamic signal acquisition and analysis system DH5927 produced by Donghua company.

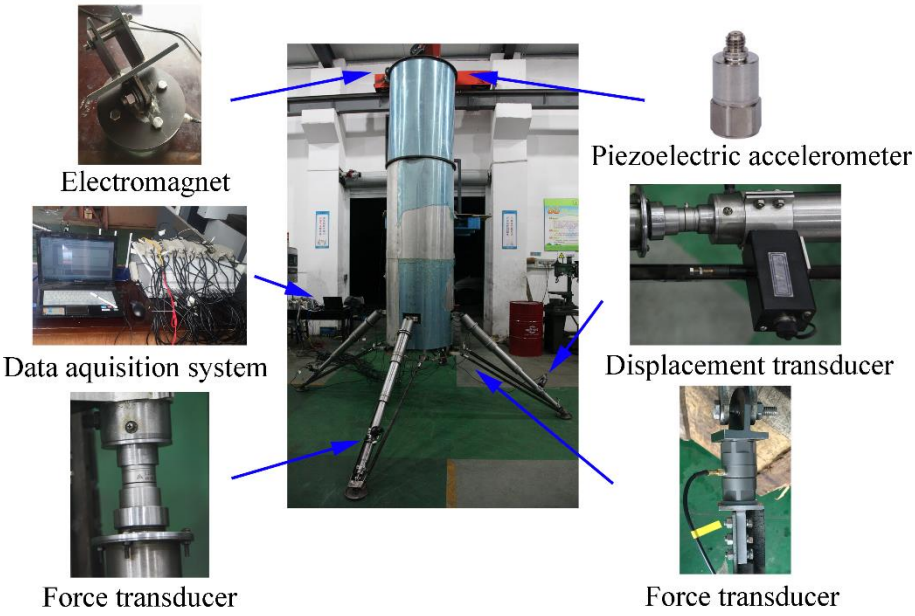

Figure 6 The drop test of the RLV main body prototype

Two landing conditions with different landing velocities are employed to test the attenuation performance of the hydraulic dampers. The distances between the footpad and ground are 4 cm and 10 cm under landing condition 1 and 2 to generate the landing velocities of 0.886 m/s and 1.4 m/s, respectively. The experiments under each landing condition are conducted twice to evaluate the test repeatability. The obtained data show that the two cases for each condition have the similar landing responses. Therefore, the results of one case under each condition are presented and analyzed in the following section. The sampling rates of the data acquisition system for all the sensors are 5000 Hz in order to record the transient changes during the landing impact.

4.2 System parameters

The complete RLV landing prototype model can be represented by equations (38) and (39). It depends on several mechanical, hydraulic, friction and contact model parameters. These parameters are obtained through direct measurements, e.g. geometry and weights, from the product specifications, e.g. standard liquid properties, from previous research, e.g. footpad-ground contact parameters, and parameter identification completed as a part of the present research, e.g. advanced compressibility, standard flow characteristics and some friction-related parameters.

The dimethyl silicone oil used in this research is PMX-200 silicone oil from the Dowing chemical company, with the kinematic viscosity reaching 100 cSt. The available parameters of the nominal liquid spring damper are summarized in Table 1. These parameters are specified under $25^{\circ}C$ and atmospheric pressure.

Table 1 The selected parameters of the liquid spring damper model

Parameters	*Value*	*Units*
Density of liquid: ρ_{liq}	960	kg/m^3
Dynamic viscosity of liquid: μ_l	9.6×10^{-3}	Pa·s
Molar mass of vaporized liquid: M_v	162	g/mol
Universal gas constant: R	8.3144	J/mol/K
Density of air: ρ_{air}	1.2	kg/m^3
Hydraulic damper cylinder diameter	50	mm
Hydraulic damper piston rod diameter	15	mm
Length of hydraulic damper cylinder	96	mm
The initial volume of lower chamber: V_{01}	1.77×10^5	mm^3
The initial volume of upper chamber: V_{02}	1.79×10^3	mm^3
Orifice length: l_h	6	mm
Orifice area: A_o	$2\times\phi2.3$	mm^2
Orifice jet contraction coefficient: C_c	0.8	
The gas polytropic exponent: γ	1.0 (quasi-static condition) 1.1 (dynamic condition [23])	

The available parameters of the vehicle's main structure, as determined through the direct measurements on the test prototype, are summarized in Table 2.

Table 2 The parameters of the vehicle's structure

Parameters	*Value*	*Units*
Mass of the upper mass, m_u	44.5	kg
Mass of the lower mass, m_d	4.2	kg
The distance between the main-body gravity center and connection point of the main strut in vertical direction, h_u	1.103	m
The distance between the main-body gravity center and	0.445	m

connection point of the main strut in horizontal direction, l_u		
The distance between the main-body gravity center and connection point of the auxiliary strut in vertical direction, h_d	1.513	m
The distance between the main-body gravity center and connection point of the auxiliary strut in horizontal direction, l_d	0.463	m
Length of main strut at fully extended position, l_{p0}	1.426	m
Length of auxiliary strut at fully extended position, l_{a0}	1.145	m
Effective area of the auxiliary strut, A_{eff}	5.91×10^{-4}	m^2
Rake angle of the main strut, θ	46.6	°
Rake angle of the auxiliary strut, φ	33.0	°

The parameters a_r and b_{strib} in the friction model of the liquid spring damper are based on [36], while the parameters in the auxiliary strut force and the contact force between the ground and footpad are determined based on previous research [37] and [38]. The typical range for the damping ratio of a steel and jointed auxiliary strut is assumed to be in the range between 0.03 and 0.3 [39]. Through correlating the 3-DOF model's auxiliary strut forces for several damping ratios from this range with the corresponding experimentally measured forces, the value 0.2 is chosen for all following studies. The parameter values are summarized in Table 3.

Table 3 The parameters in damper friction, auxiliary strut and contact force models

Parameters	*Value*	*Units*
Increase ratio of friction force during sticking mode, a_r	0.25	
The constant of the Stribeck effect, b_{strib}	0.001	m/s
The elastic modulus of auxiliary strut material, E_a	206	GPa
The damping ratio of the auxiliary strut, η	0.2	
The exponential coefficient of the auxiliary strut force, e_k	2	
The spring constant of the ground contact force, K_g	1×10^8	N/m
The maximum damping coefficient of ground contact, $C_{g\max}$	1×10^4	N/m/s
The minimum penetration depth corresponding to the maximum damping coefficient, δ_{pen}	1×10^{-4}	m
The exponential coefficient of penetration depth, e_n	1.5	
The friction coefficient of footpad-ground contact, μ_c	0.2	

4.3 Parameter identification

The quasi-static tests are performed individually on the four custom manufactured and nominally identical liquid spring dampers. These tests are used to identify the unknown compressibility parameters; namely the air content $x_a(P_{atm})$, liquid bulk modulus $B_{liq}(P_{atm})$, slope of the liquid bulk modulus change with pressure C_B; and the damper friction parameters; namely the initial spring rate of friction force K_{r0}, slope of the spring rate change with pressure C_K, displacement threshold of the friction force s_{r0}, damping coefficient during the sticking mode C_r. The damper compression and extension tests at the speed of 0.2 mm/s are used to produce suitable damper response data. This low-speed test condition ensures that the measured forces are influenced mainly by the friction and compressibility driven phenomena, while other damping and inertial effects are minimized. The displacement range of the tests are [0 mm, 38 mm] and the sampling rates are 30 Hz. Two cycles of compression and extension are conducted for each damper and the data for the last cycle are recorded and presented.

The dynamic drop tests of the RLV test prototype produce highly dynamic responses due to landing impact conditions. These tests are completed under varying conditions to enable two separate analyses. First, the experimental displacements measured across the dampers in the landing legs and their velocities, which are derived from the corresponding displacement signals, are employed directly as the inputs to the local damper model to calculate the simulated forces. By doing this, the modelling uncertainty associated with the main-structure flexibility, the nonlinear and unmodeled effects can be excluded from the damper force calculations. Any resulting discrepancies can then be primarily attributed to the damper modelling uncertainty. The comparison between the measured and simulated axial force responses is used to identify the orifice discharge coefficient C_d. After this, the same drop test data are used to evaluate the simulation performance of the full model during the equivalent landing conditions. The main aim of this study is to provide understanding of the extent and nature of the experiment-simulation discrepancies arising from the unmodeled overall physics. The drop tests are performed for two different impact conditions with drop height getting to 4 cm and 10 cm, respectively.

To support the quantitative comparative analyses between the measured and predicted responses, the relative Root Mean Square (RMS) value of the response residuals R_{RMS} [40] is used

$$R_{RMS}(\mathbf{p}) = \frac{\sqrt{\frac{1}{m}\sum_{i=1}^{m}(U_{mod}(t_i,\mathbf{p}) - U_{exp}(t_i))^2}}{\sqrt{\frac{1}{m}\sum_{i=1}^{m}U_{exp}^2(t_i)}} \tag{40}$$

where $U_{mod}(t_i,\mathbf{p})$ represents the simulated data, $\mathbf{p}$ is the vector of selected model parameters, U_{exp} represents the experimental data, m is the number of the recorded sampling time instants t_i.

Having established the measure of the simulation-experiment difference through R_{RMS} in equation (40), parameter identification can be completed through minimization of this measure. The standard minimization problem is formulated as follows

$$\min_{\mathbf{p}\in D}\sum_{(j)} R_{RMS,j}(\mathbf{p}) \rightarrow \mathbf{p}_{id} \tag{41}$$

where $D \subset \mathbb{R}^{N_P}$, D is the parameter search subdomain for the case with N_P independent model parameters and j represents any possible individual test instances combined into a single parameter identification scenario.

The actual minimization problem is solved using the local optimization solver *fminsearch* in Matlab environment [35] with the default setup. The initial values of damper parameters for optimization under quasi-static condition are $[x_a, B_{liq}, C_B, K_{r0}, C_K, s_{r0}, C_r]$=[0.15, 1×10^9, 10, 3×10^5, 1×10^{-2}, 5×10^{-4}, 100], while the initial value of C_d under impact condition is 0.7.

The results of the analyses described in this section are summarized in the following tables and figures. The identified damper parameter values are shown in Table 4. The final R_{RMS} values for the damper forces and their enhancement after optimization are provided in Table 5. The comparison of the damper axial forces between the simulation and experiments under quasi-static condition across all tested devices are shown in Figure 7.

Table 4 The identified damper parameters

Parameters	*Damper 1*	*Damper 2*	*Damper 3*	*Damper 4*	*Mean*	*Standard deviation*
Air content (%): $x_a(P_{atm})$	0.106	0.0944	0.105	0.120	0.106	1.08×10^{-2}
Liquid bulk modulus under P_{atm} (Pa): $B_{liq}(P_{atm})$	9.74×10^8	9.64×10^8	9.97×10^8	9.93×10^8	9.82×10^8	1.54×10^7
Slope of bulk modulus change with pressure: C_B	12.12	12.69	11.21	11.28	11.83	0.68

Initial spring rate of friction (N/m): K_{r0}	2.95×10^{5}	4.69×10^{5}	3.54×10^{5}	6.29×10^{5}	4.37×10^{5}	1.39×10^{5}
Slope of spring rate change in friction(N·Pa/m): C_K	3.09×10^{-3}	5.45×10^{-3}	2.70×10^{-3}	5.61×10^{-3}	4.21×10^{-3}	1.46×10^{-3}
Displacement threshold of friction force (m): s_{r0}	4.9×10^{-4}	3.52×10^{-4}	4.84×10^{-4}	3.24×10^{-4}	4.12×10^{-4}	1×10^{-4}
Damping coefficient during sticking mode (N·s/m): C_r	102.34	214.37	113.81	104.52	133.76	49.25
Discharge coefficient of orifice: C_d	0.651	0.664	0.637	0.693	0.661	2.4×10^{-2}

The individually identified parameters for each damper, their average values and standard deviations are presented in Table 4. The average values are used in the 3-DOF dynamic model in section 5. The standard deviations reflect the degree of dispersion of the corresponding parameters across all studied dampers. It can be seen that the liquid compressibility parameters for the dampers are identified consistently, while more significant differences and identification uncertainty exists among the friction parameters. This can be exemplified by the wide dispersion in the identified values of the damping coefficient during sticking mode C_r.

Table 5 The R_{RMS} values of the damper forces and their enhancement after optimization under different test conditions

Damper / Test		Quasi-static test	Condition 1	Condition 2
Damper 1	R_{RMS} *(%)*	0.449	8.66	14.09
	Enhancement (%)	88.72	15.68	-6.99
Damper 2	R_{RMS} *(%)*	0.463	7.92	10.10
	Enhancement (%)	89.81	3.18	2.04
Damper 3	R_{RMS} *(%)*	0.701	8.91	10.83
	Enhancement (%)	85.73	5.11	8.14
Damper 4	R_{RMS} *(%)*	0.65	10.06	12.63
	Enhancement (%)	81.17	0.98	1.48

Note: "Enhancement" in Table 5 represents the R_{RMS} reduction after optimization. A positive value

represents an improved prediction, while a negative value represents a worse prediction.

Table 5 shows that the R_{RMS} values of all four dampers under the chosen quasi-static conditions are less than 0.8 %. Further, they are under 11% for landing condition 1 and under 15% for landing condition 2. This represents a good accuracy of the local damper model. The R_{RMS} enhancement under the quasi-static conditions for four dampers is above 80%, demonstrating the positive effect of optimization. Through comparison between the initial and optimized parameter values, it can be seen that the air content $x_a(P_{atm})$ is a particularly important factor under the quasi-static condition. The R_{RMS} values for damper 2, 3 and 4 under conditions 1 and 2 are also improved slightly. Because C_d is optimized based on the combined R_{RMS} under condition 1 and 2, R_{RMS} of damper 1 under condition 1 decreases by 15.68 % after optimization, while R_{RMS} for condition 2 increases by 6.99 %.

Figure 7 shows the comparison between experiment and simulation with the final identified damper parameters under the quasi-static condition. A positive value of force represents the damper under quasi-static compression.

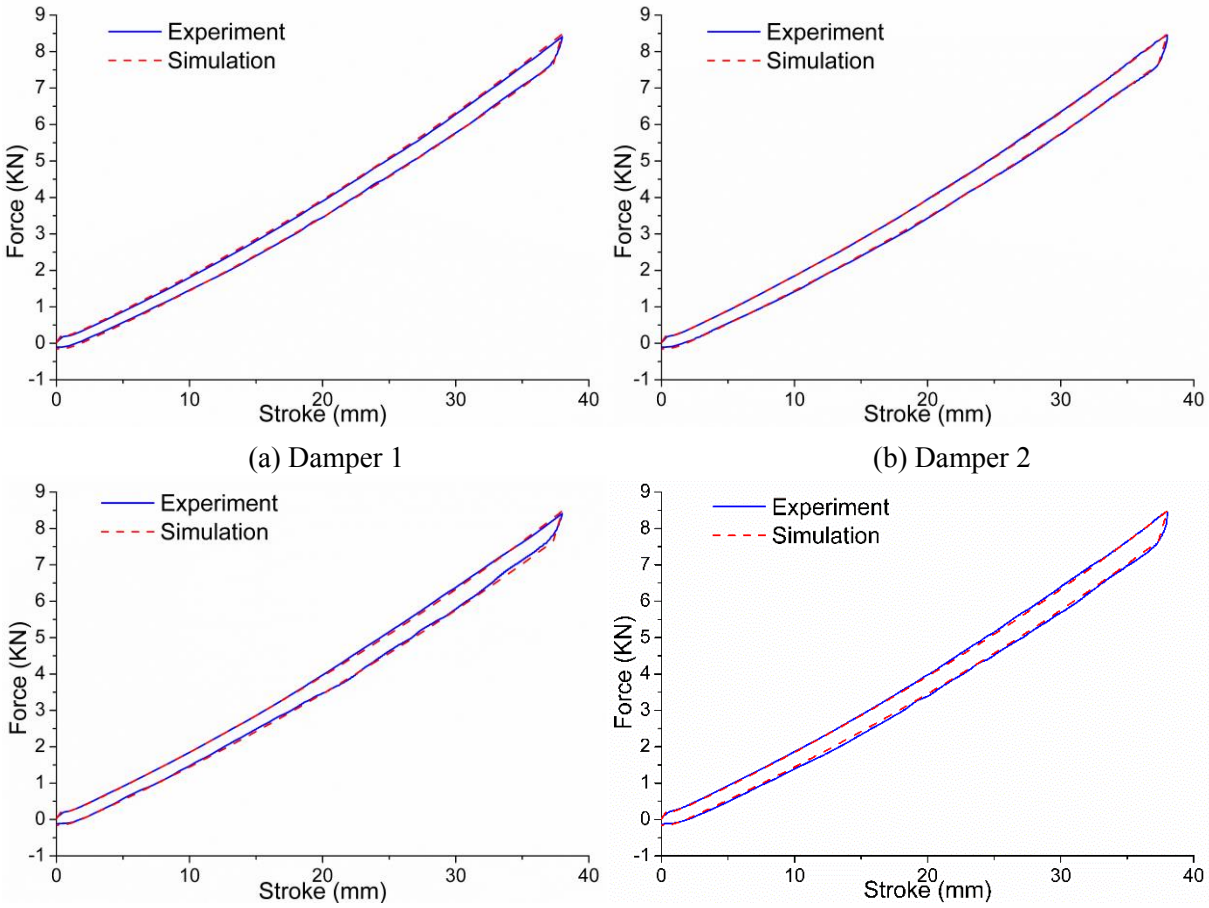

Figure 7 The comparison of damper forces between simulation and experiment under quasi-static condition

It can be seen in Figure 7 that the slopes of the experimental and simulated responses are both increasing nonlinearly with the stroke, which is caused by the growth of the bulk modulus with increasing pressure. The presence of this behavior across the full loading range indicates that the bulk modulus change with pressure C_B is an essential parameter for this liquid spring damper model. Although the discrepancy due to the friction model still exists during the motion transition from the damper compression to extension, overall, the predicted curves can properly represent the increase in the damper force with increasing chamber pressures. These results also indicate acceptable machining tolerances, assembly repeatability and liquid filling reliability for all four dampers as well as good predictive capability of the simulation model.

Having the damper compressibility and friction parameters identified, in the next step, the displacements across all four dampers measured under landing condition 1 and 2 are used to obtain the

flow parameter C_d using equations (40) and (41). To provide suitable inputs for this analysis, the measured displacement signals are processed with the Savitzky-Golay polynomial smoothing and differentiation filters implemented in MATLAB [35]. The damper velocities are computed by differentiating the corresponding smoothed displacement signals with time using the same filter. Different settings of the number of samples in the sliding data subset window for the Savitzky-Golay filter are chosen to smooth the measured displacements and velocities of damper 1, which are then employed as inputs for calculating the damper force. From this study, the polynomial order of the Savitzky-Golay filter is set to 2. The comparison of the displacement and velocity curves filtered with different sample size setting are shown in the top and middle subplots of Figure 8. The corresponding damper forces are shown in the bottom subplot of Figure 8. The raw experimental force data in this subplot is measured by the force transducer during the drop test.

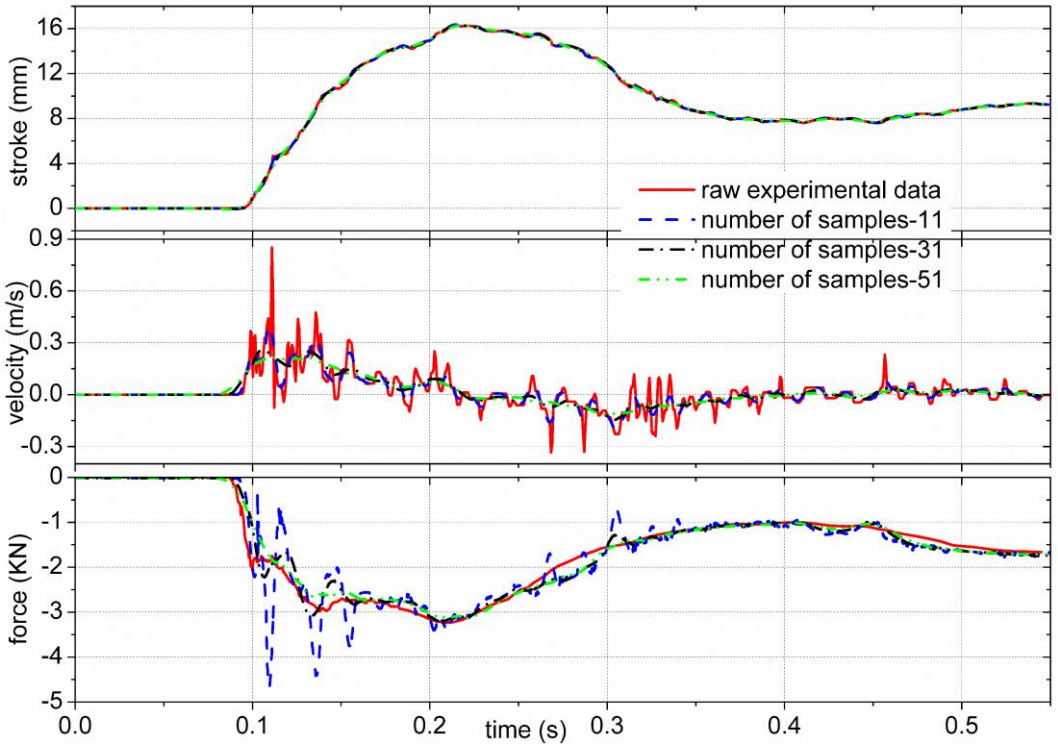

Figure 8 The comparison of the displacement, velocity and force curves of damper 1 with different smoothing parameters

From Figure 8, with the filter sampling window sizes increasing from 11 to 51, the displacement and velocity curves are getting smoother. The velocity curve obtained from the raw experimental data has significantly larger oscillations than the filtered velocity curves which is caused by the vibration of the structure and the displacement sensor. Because of this, and for better interpretation of the results, the

damper force obtained when using the raw experimental data inputs is not shown in the third subplot of Figure 8. In the third subplot, the damper forces obtained with the inputs filtered by 31 and 51 samples are closer to the experimental force than the case with 11 samples. The curve with 51 samples is slightly over-smoothed. Therefore, the data points of 31 samples is used for filtering the experimental displacement and velocity data across all dampers.

After determining the suitable parameters of the Savitzky-Golay filter, the measured and processed damper displacement and velocity data under two landing conditions are shown in Figure 9.

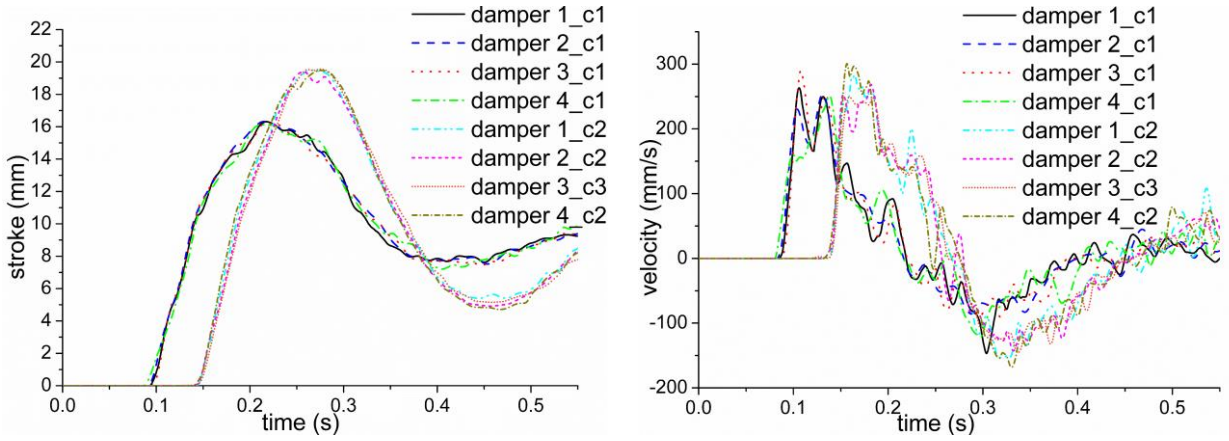

(a) piston strokes (b) piston velocities

Figure 9 The smoothed experimental piston strokes and velocities across the dampers

From Figure 9(a), the displacements of four dampers under condition 1 reach their peaks at approximately 0.215 s, while the displacements under condition 2 reach their peak at 0.268 s. The rebound height, which is the distance between the first peak and the first valley of the stroke, is approximately 8.79 mm under condition 1, while the rebound height reaches approximately 14.37 mm due to larger initial landing velocity. In addition, high frequency oscillations are observed in the obtained damper displacements and velocities. These effects can be associated with the impact-induced parasitic transversal loading of the displacement transducer or the damper itself during the drop tests. Alternatively, these oscillatory effects can be attributed to the flexibility of the vehicle's main body. Overall, the displacements and velocities of four dampers have the same general shape, which demonstrates that the RLV prototype lands vertically during the tests with no significant tilt angles. The landing gear system, therefore, can be assumed to be symmetric with symmetric loading.

With the filtered experimental displacements and velocities used as inputs, the response forces of the local damper model can be obtained and compared with the experimental damper forces. This comparison between the forces is shown in Figure 10. In these figures, a negative value of the force represents the damper under compression, while a positive value represents the damper under tension.

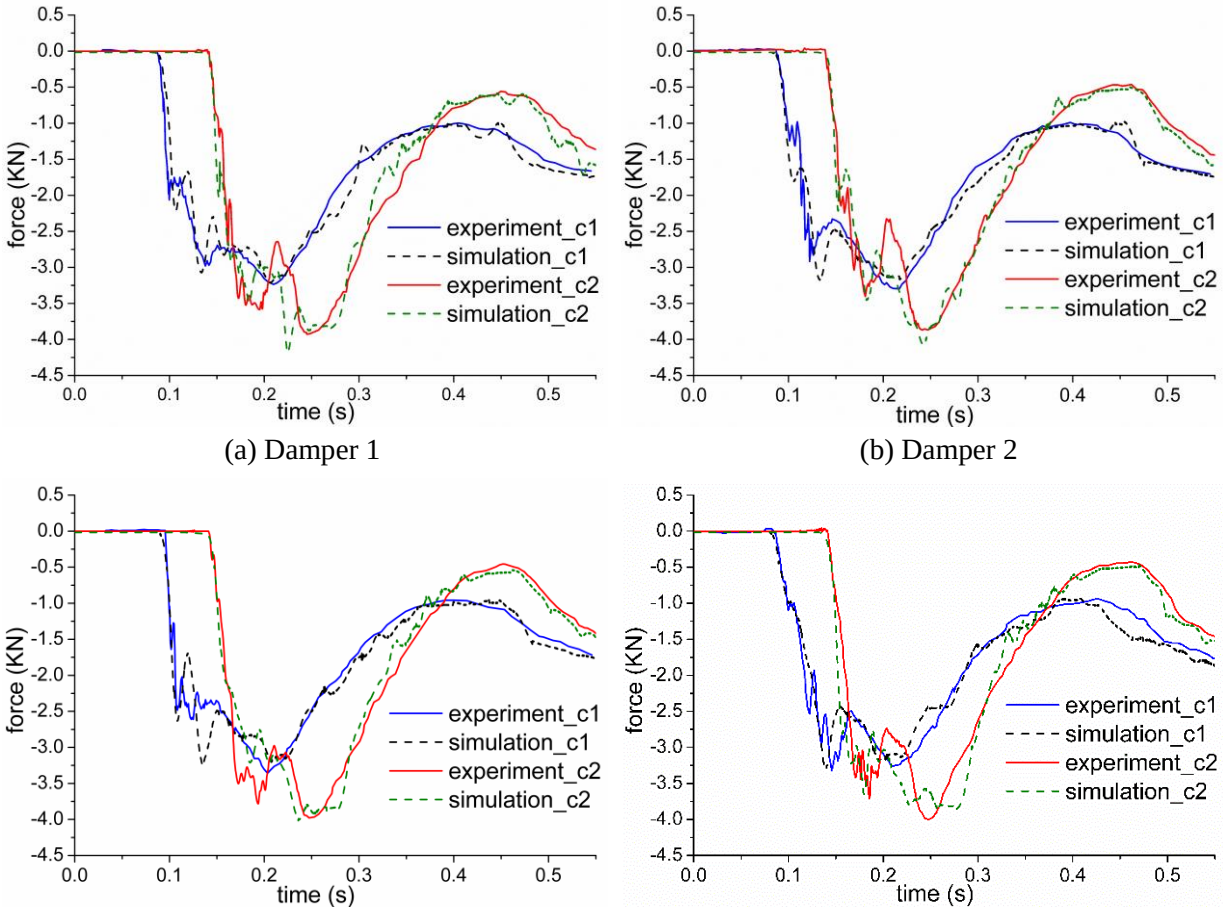

(a) Damper 1 (b) Damper 2

(c) Damper 3 (d) Damper 4

Figure 10 Comparison of the simulated and experimental damper forces under landing condition 1 and 2

From Figure 10, both simulated and experimental force curves have two major peaks, which are approximately 2900 N and 3300 N for condition 1 and 3500 N and 3900 N for condition 2. The first peak occurs at the beginning of the touchdown phase due to the sudden increase of the pressure difference between the working chambers, while the second peak happens soon after this event and before the rebound phase and it can be associated with the fluid compressibility properties. In addition, the slight force oscillations are observed in both experimental and simulated curves. For the experimental curves, it is thought that these effects are caused by the structural flexibility and nonlinear

contact effects in the full tested RLV prototype. For the simulated curves, these effects result from the high-frequency oscillations present in the smoothed and differentiated experimental displacements and velocities which are used as the excitation inputs in the local damper model studies.

5 Dynamic model validation

The above analysis is aimed at establishing the reference and reliable liquid spring damper model which can predict the local measured damper responses. In this section, the focus is moved on to the simulation and response evaluation of the full RLV model. The established 3-DOF model under two previously described landing conditions is compared with the experimental data represented by the vehicle's vertical accelerations and the main and auxiliary strut forces.

Figure 11 shows the comparison between the simulated and experimental damper forces under the tested landing condition 1 and 2. Similarly, Figure 12 shows the damper forces versus the corresponding damper strokes under these landing conditions. The blue and red curves represent the average of the four dampers forces obtained from the experiment and local damper model simulations, respectively. The black curves represent the damper forces obtained from the 3-DOF model landing simulations. This configuration therefore enables both experiment-simulation as well as local-global simulation comparisons.

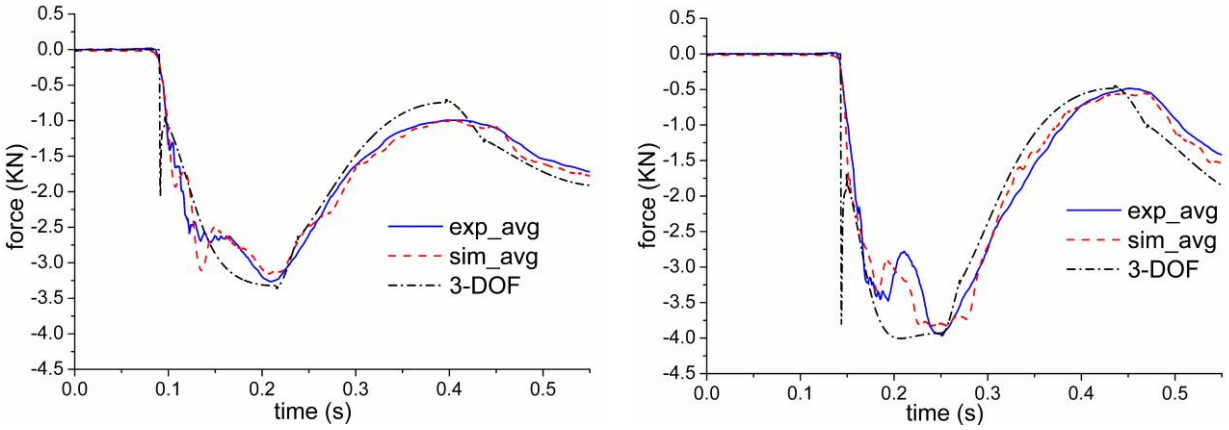

(a) Landing condition 1 (b) Landing condition 2

Figure 11 Comparison of the measured and simulated damper forces from the full 3-DOF drop simulation under different conditions

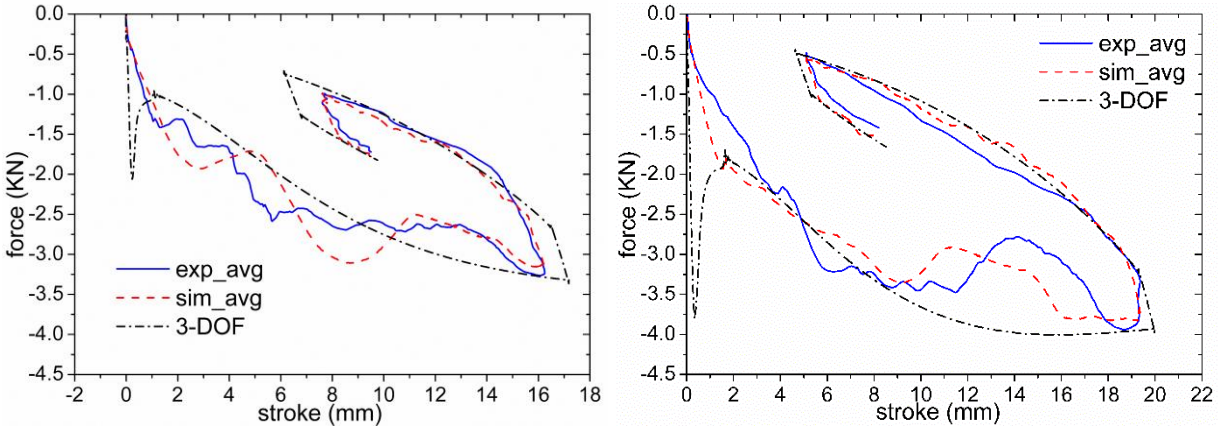

(a) Landing condition 1 (b) Landing condition 2

Figure 12 Comparison of the measured and simulated damper forces versus piston strokes under different conditions

From Figure 11(a), the forces from the 3-DOF model simulation reach the first valley (-2059.4 N) at the touchdown instant and, after this, they rebound to smaller absolute values earlier than the experimental results. The reason behind this behavior is the influence of the unmodeled physics manifested by the full RLV model's lack of additional flexibilities in the main structure and landing legs. After this touchdown, the 3-DOF model response progresses gradually from -1035.7 N at 0.097 s to the second valley at 0.216 s. This response is different from the experimental curve which shows more complex behavior with two additional valleys at approximately 0.134 s and 0.211 s. Similarly, from Figure 11(b), the force from the 3-DOF model simulation changes gradually after the initial rapid and exaggerated touchdown event. Then, it experiences a force plateau between 0.194 s and 0.253 s. Like condition 1, the rebound event of the 3-DOF model under condition 2 occurs 0.014 s earlier than the corresponding experimental curve. In addition, the peak force under condition 2 is approximately -3941.1 N, which is 677.9 N lower than that under condition 1. From Figure 12, the damper force of the 3-DOF model experiences a sudden increase during the initial touchdown event, while the damper forces of the local damper model and experiments increase more gradually and then fluctuate during the whole compression period due to the structural flexibility and nonlinear impact effects. Additionally, both the experimental and simulated peak forces and displacements experience a significant increase with the growing initial landing velocity.

In addition, the local damper-based responses with the experimental stroke and velocity inputs are substantially closer to the experimental force curves than the equivalent curves obtained from the full

3-DOF model simulations. This suggests that the influence of unmodeled physics such as the structural flexibilities, gaps in the joints and the nonlinear contact conditions produce the discrepancies between the experimental and 3-DOF model curves.

Figure 13 shows the comparison between the simulated and experimental auxiliary strut forces under condition 1 and 2. In this figure, a negative value of the force represents the auxiliary strut under compressive load while a positive value represents the auxiliary strut is under tensile load.

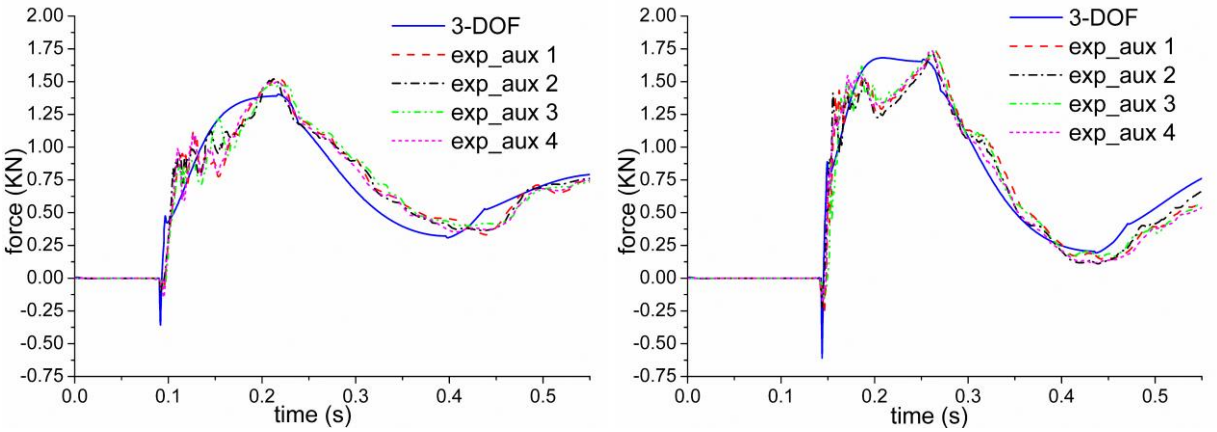

(a) Landing condition 1 (b) Landing condition 2

Figure 13 Comparison between the simulated and experimental auxiliary strut forces under different landing conditions

Compressive load is observed in the auxiliary struts at the touchdown instant, both in simulation and experiment, after which it changes and remains in the tensile region. Despite slight oscillations during the initial touchdown instant, the experimental forces of all four auxiliary struts and the simulation forces have the same general profile under conditions 1 and 2. The maximum predicted force under condition 1 reaches 1403.5 N which is 7.19% smaller than the experimental peak response while the maximum predicted force under condition 2 reaches 1681.7 N which is only 3.02% smaller than the experimental peak load. As in the case of the main landing strut, the absence of the high-frequency oscillations and early rebound are observed in the responses of the 3-DOF model due to the unmodelled structural flexibilities and nonlinear effects in joints.

Figure 14 is used to demonstrate the differences between the modelled and experimentally observed vertical accelerations of the tested RLV structure under landing condition 1 and 2. Due to the influence of the high frequency response of the tested system, the experimental accelerations are shown in their low pass filtered form. The chosen low-pass filter cut-off frequency is 100 Hz.

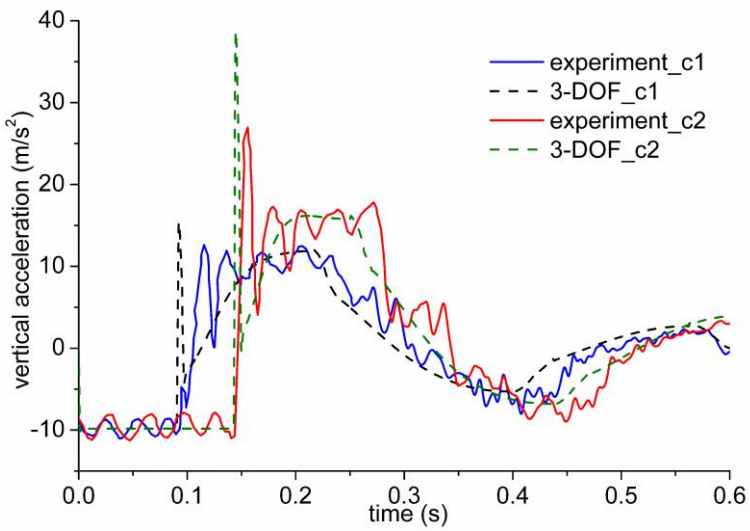

Figure 14 Comparison of the vertical accelerations between simulation and experiment under condition 1 and 2

As already observed for the force responses and attributed to the unmodeled physics, the 3-DOF RLV model accelerations for both landing conditions reach their increased peaks at the touchdown instants which occur at 0.0923 s and 0.145 s, respectively. The lower experimental peak accelerations appear at the delayed time instants of 0.115 s and 0.156 s, respectively. Additionally, when excluding the effect of high frequency oscillations, the accelerations during time intervals of [0.127 s, 0.239 s] in condition 1 and [0.170 s, 0.281 s] in condition 2 for both experimental and 3-DOF RLV model cases remain stable and then decrease gradually to their equilibrium states. The pre-impact oscillations of the experimental curves can be observed during [0 s, 0.094 s] for condition 1 and [0 s, 0.144 s] for condition 2, which result from the transient response introduced initially by the sudden release of the model RLV structure during its drop tests. Being recorded by an accelerometer which is mounted on top of the flexible main body, these high frequency oscillations are present in the experimental curves for both landing conditions during the full landing event. In contrast, because this feature is not modelled in the 3-DOF RLV model, these oscillations are not present in the predicted acceleration response curves.

Table 6 quantifies the global predictive capability of the full 3-DOF RLV prototype model with the help of the R_{RMS} measure introduced in equation (40). The experimental values of the main strut force, auxiliary strut force and main strut stroke are taken as the mean values of the four landing legs and then compared with the predicted values.

Table 6 Summary comparison between the full 3-DOF RLV simulations and drop experiments

Landing responses		Main strut stroke	Main strut force	Auxiliary strut force	Vertical acceleration
R_{RMS} (%)	Condition 1	9.28	12.54	16.11	41.30
	Condition 2	10.81	22.32	15.73	48.89

From Table 6, the R_{RMS} values of the force and main strut stroke responses under condition 1 and 2 are less than 23 %. The vertical accelerations have their R_{RMS} values below 49 %. This discrepancy is caused by the simplified nature of the full 3-DOF RLV model which does not include the elasticity of the main-structure and potentially highly influential nonlinear contact between the part of the RLV prototype assembly.

6. Conclusion

This paper establishes a new nonlinear lumped parameter model of liquid spring damper and a 3-DOF model of vertical landing RLV test prototype. This model considers the variable fluid bulk modulus, entrapped air, fluid flow inertial effects and cavitation. The damper parameters concerning the fluid compressibility and friction between the cylinder and piston rod are identified through quasi-static compression tests for a group of four custom-manufactured and nominally identical liquid spring dampers. Then the orifice flow coefficients of the tested dampers are estimated from the vehicle drop test data. After that, the full 3-DOF RLV simulation model is studied and compared with the drop test experimental data under two different landing conditions.

The predictive capability, expressed in terms of the Root Mean Square error, changes from less than 1% for the quasi-static force predictions to 9%-12% for the local damper dynamic force predictions and then to 10%-50% error range for the full 3-DOF RLV simulations. The lower ends of the error ranges are dominated by the lower landing velocity cases and the force and stroke predictions, e.g. 9% local damper force error during the low speed landing case, while the higher errors are linked with the high-speed landing accelerations, i.e. 50% high speed landing acceleration error. The primary source of the 3-DOF RLV model prediction errors, between 10% and 50%, is attributed to unmodelled physics,

e.g. main body's structural and joint contact flexibilities. Additionally, an excessive effective stiffness in this model causes the unrealistic touch-down force responses which can be eliminated by increasing fidelity of the full landing model. The source of the errors in the local damper studies, between 9% and 12% for the drop tests and around 1% for the quasi-static test, are caused by the parameter and piston motion identification uncertainties. The compressibility model and its parameters, in particular air content and slope of bulk modulus change with pressure, enable the achieved 1% error in the quasi-static damper force predictions with moderate cross-damper parameter variability of around 10%. The friction parameters, owing to their localized influence within the full loading range, have only minor influence on the resulting RMS errors whilst maintain significant cross-damper variability at 30-40% of their values. Finally, the orifice discharge coefficient is identified consistently for all four dampers with 4% cross-damper variability while it changed only by 6% relative to its initial value.

Generally, the liquid spring damper model developed and evaluated in this work can represent the observed experimental behavior with acceptable discrepancies. The adopted approach provides the low order damper and RLV models while maintaining close links with the performance-critical physical principles, which makes them suitable for future more detailed studies such as asymmetric landing, and other critical performance.

Acknowledgements

This work was supported by Postgraduate Research & Practice Innovation Program of Jiangsu Province [grant number KYCX17_0275]; the fund of China Scholarship Council [201706830015]; and the Priority Academic Program Development of Jiangsu Higher Education Institutions.

References

[1] S. Yue, H. Nie, M. Zhang, M.Y. Huang, H. Zhu, D. Xu, Dynamic analysis for vertical soft landing of reusable launch vehicle with landing strut flexibility. P. I. Mech. Eng. G.-J. Aer., 0954410017753209 (2018).

[2] X. Wei, Q. Lin, H. Nie, M. Zhang, J. Ren, Investigation on soft-landing dynamics of four-legged lunar lander, Acta Astronaut., 101(1) (2014) 55-66.

[3] S. Yue, H. Nie, M. Zhang, M.Y. Huang, H. Zhu, D. Xu, Optimization and performance analysis of oleo-honeycomb damper used in vertical landing reusable launch vehicle, J. Aerospace Eng. 31(2) (2018) 04018002.

[4] L. Witte, Touchdown dynamics and the probability of terrain related failure of planetary landing systems-a contribution to the landing safety assessment process (Doctoral dissertation), University of Bremen, 2015.

[5] Y.T. Choi, R. Robinson, W. Hu, N.M. Wereley, T.S. Birchette, A.O. Bolukbasi, J. Woodhouse, Analysis and control of a magnetorheological landing gear system for a helicopter, J. Am. Helicopter Soc. 61(3) (2016) 1-8.

[6] Y. Kushida, S. Hara, M. Otsuki, Y. Yamada, T. Hashimoto, T. Kubota, Robust landing gear system based on a hybrid momentum exchange impact damper, J. Guid. Control Dynam., 36(3) (2013) 776-789.

[7] W.S. Gullotta, C.G. Kirchner, A.P. Yuengert, P.A. Zink, Resettable Landing Gear for Mars Hopper, in: 11th International Planetary Probe Workshop, Pasadena, CA, USA, 2014.

[8] F. B. Sperling, The Surveyor shock absorber, Proc., 3rd Aerospace Mechanisms Symp., N50–17368, National Aeronautics and Space Administration, Hampton, VA., 1968.

[9] S.R. Hong, G. Wang, W. Hu, N.M. Werely, Liquid spring shock absorber with controllable magnetorheological damping, P. I. Mech. Eng. D.-J. Aut., 220(8) (2006) 1019-1029.

[10] A.K. Samantaray, Modelling and analysis of preloaded liquid spring/damper shock absorbers, Simul. Model. Pract. Th., 17(1) (2009) 309-325.

[11] P. Raja, X. Wang, F. Gordaninejad, A high-force controllable MR fluid damper–liquid spring suspension system, Smart Mater. Struct., 23(1) (2013) 015021.

[12] W.A. Welsh, Simulation and correlation of a helicopter air-oil strut dynamic response, The 43th Annual Forum of the American Helicopter Society, St. Louis, Missouri, May 18-20, 1987

[13] A. Farjoud, M. Ahmadian, M. Craft, W. Burke, Nonlinear modelling and experimental characterization of hydraulic dampers: effects of shim stack and orifice parameters on damper performance, Nonlinear Dyn., 67(2) (2012) 1437-1456.

[14] X. Liu, J.Z. Jiang, Titurus B., A. Harrison, Model identification methodology for fluid-based inerters, Mech. Syst. Signal Pr., 106 (2018) 479-494.

[15] B. Titurus, J. Du Bois, Lieven N., Modelling and testing of a semiactive hydraulic damper in periodic working regimes, AIAA J., 50(4) (2012) 844-854.

[16] B. Titurus, J. Du Bois, N. Lieven, R. Hansford, A method for the identification of hydraulic damper characteristics from steady velocity inputs, Mech. Syst. Signal Pr., 24(8) (2010) 2868-2887.

[17] H. Gholizadeh, D. Bitner D., R. Burton, G. Schoenau, Modelling and experimental validation of the effective bulk modulus of a mixture of hydraulic oil and air, J. Dyn. Syst.-T. ASME, 136(5) (2014) 051013.

[18] W.L. Wang, D.S. Yu, Z. Zhou, In-service parametric modelling a rail vehicle's axle-box hydraulic damper for high-speed transit problems, Mech. Syst. Signal Pr., 62 (2015) 517-533.

[19] J. Zhou, J. Hu, C. Jing, Lumped parameter modelling of cavitating orifice flow in hydraulic systems, Stroj. Vestn.-J. Mech. E., 62(6) (2016) 373-380.

[20] K. Lee, Numerical modelling for the hydraulic performance prediction of automotive monotube dampers, Vehicle Syst. Dyn., 28(1) (1997) 25-39.

[21] F.R. Young, Cavitation, World Scientific, 1999.

[22] M. Alonso, Á. Comas, Thermal model of a twin-tube cavitating shock absorber, P. I. Mech. Eng. D.-J. Aut., 222(11) (2008) 1955-1964.

[23] N.S. Currey, Aircraft landing gear design: principles and practices, AIAA, 1988.

[24] B. Titurus, N. Lieven, Modelling and analysis of semi-active dampers in periodic working environments, AIAA J., 47(10) (2009) 2404-2416.

[25] D.S. Weaver, S. Ziada, A theoretical model for self-excited vibrations in hydraulic gates, valves and seals, J. Press. Vess.-T. ASME, 102(2) (1980) 146-151.

[26] M. Mao, W. Hu, Y.T. Choi, A.L. Browne, J. Ulicny, N. Johnson, Nonlinear modelling of magnetorheological energy absorbers under impact conditions, Smart Mater. Struct., 22(11) (2013) 115015.

[27] F. Luo, X. Zhang, A Review of aeration and cavitation phenomena in the hydraulic shock absorber, Appl. Mech. Mater., 2014.

[28] V. Hopkins, D.R. Wilson, C. Bolze, Isothermal Bulk Modulus of selected fluids to 700 F and 10,000 psig, J. Basic Eng., 86(3) (1964) 463-467.

[29] H. Gholizadeh, R. Burton, G. Schoenau, Fluid bulk modulus: comparison of low pressure models, Int. J. fluid power, 13(1) (2012) 7-16.

[30] A.A. Younan A.A., J. Cao, T.W. Dimond, P.E. Allaire, Nonlinear analysis of squeeze film damper with entrained air in rotordynamic systems. Tribol. T., 54(1) (2010) 132-144.

[31] Z.A. Khan, V. Chacko, H. Nazir, A review of friction models in interacting joints for durability design, Friction, 5(1) (2017) 1-22.

[32] E. Pennestrì, V. Rossi, P. Salvini P., P.P. valentini, Review and comparison of dry friction force models, Nonlinear Dyn., 83(4) (2016) 1785-1801.

[33] C.J. Liao, W.F. Huang, Y.M. Wang, S.F. Suo, X.F. Liu, Optimization design for mechanical seals in reactor coolant pumps based on a fluid–solid strong-interaction model, P. I. Mech. Eng. C-J. Mec., 225(8) (2011) 1851-1862.

[34] T. Maeda, M. Otsuki, T. Hashimoto, Protection against overturning of a lunar-planetary lander using a controlled landing gear, P. I. Mech. Eng. G-J. Aer., (2017) 0954410017742931.

[35] MATLAB, Software Package, Ver. 2017b, MathWorks, Natick, MA, 2017.

[36] D.A. Haessig, B. Friedland, On the modelling and simulation of friction. J. Dyn. Syst.-T. ASME, 113(3) (1991) 354-362.

[37] X. Wang, H. Yao, G. Zheng, Enhancing the isolation performance by a nonlinear secondary spring in the Zener model. Nonlinear Dyn., 87(4) (2017) 2483-2495.

[38] M. Nohmi, A. Miyahara, Modelling for lunar lander by mechanical dynamics software, AIAA Modelling and Simulation Technologies Conference and Exhibit. (2005) 6416.

[39] A. Adams, A. Askenazi, Building better products with finite element analysis. OnWord Press, 1999.

[40] S.W. Duym, Simulation tools, modelling and identification, for an automotive shock absorber in the context of vehicle dynamics, Vehicle Syst. Dyn. 33(4) (2000) 261-285.